Performances of Double-Sided Silicon Strip Detectors for the ALICE experiment at LHC

F. Retière, A. Boucham, S. Bouvier, L. Conin, B. Erazmus,
S. Giliberto, B. Guillet, G. Guilloux, F. Lefevre, C. Le Moal,
L. Martin, T. Milletto, W. Pinganaud, O. Ravel, C. Roy, D. Roy

SUBATECH
UMR Ecole des Mines de Nantes, IN2P3/CNRS, Université de Nantes
4, rue Alfred Kastler, La Chantrerie, BP 20722, 44307 Nantes Cedex 3, France

Abstract

The two outermost layers of the ALICE Inner Tracking System will be equipped with double-sided silicon strip detectors. In order to analyse the behaviour of the detectors as well as readout electronics, beam-tests have been performed at SPS and PS. Detailed results are presented and compared with simulations.

Contents

1 Introduction **3**

2 Experimental setup **3**
2.1 Tested detectors and readout electronics 3
2.2 Test beam setup 3

3 Test beam results **4**
3.1 Single-side performances 4
3.1.1 Signal, noise and signal-to-noise ratios 4
3.1.2 Efficiency 6
3.1.3 Resolution at normal incidence 6
3.1.4 Optimisation of the cluster position reconstruction using the η algorithm 7
3.1.5 Resolution as a function of the incident angle 8
3.1.6 Two-track resolution 8
3.2 Reconstruction of the impact point using both sides of the detector . 11
3.2.1 Spatial resolutions 11
3.2.2 Study of the charge correlation between P and N sides. . . . 11

4 Simulation of the silicon strip detector and comparison with data 13
4.1 Model of the charge sharing process 13
4.2 Comparison with data 15
4.3 Results of the simulation 17

5 Conclusion **18**

1 Introduction

The ALICE Inner Tracking System consists of six silicon detector layers. Its main purposes are to measure low transverse momentum particles and to reconstruct short life particles via their decay. This requires a good two-dimensional spatial resolution in particular in the bending plane. In addition, the high multiplicity of particle yield in the Pb-Pb collision at LHC energies imposes a good detector granularity.

The four inner layers of the ITS will be equipped with silicon pixel and silicon drift detectors because they are true two-dimension detectors and hence able to cope with the high occupancy close to the collision point. The two outermost layers, located at radii 40 cm and 45 cm will be made of double-sided silicon strip detectors. The occupancy at these radii is low enough to allow the measurement of the impact points in two dimensions by associating the positions measured by two one-dimension detectors represented by each side of the double-sided detector.

In section 2, we briefly describe the experimental setup used during the test beam.

In section 3, we report on the results obtained on test-beam data, first when each side of the detector is considered separately and then when both sides are associated.

In section 4, we describe a model which has been developed to reproduce the detector behaviour and compare the simulation results with data.

2 Experimental setup

2.1 Tested detectors and readout electronics

Two sets of detectors provided by two different manufacturers, Canberra and Eurysis, have been tested. These detectors, designed according to the ALICE Technical Proposal [1], were equipped with two different front end electronics : the ALICE 128C chips [4] designed especially for ALICE and classical VA2 chips [3]. Results on off-beam and in-beam tests of the detectors equipped with ALICE 128C chips have been published in [2].

The ALICE 128C chip is controled by JTAG and has been designed to provide a low noise in the capacitance range of the silicon strip detector but also to limit the power consumption in order to minimize cooling issues and to enlarge the dynamics of the VA2 chip by a factor two.

A schematic view of the detector is shown in figure 1: it is 42 mm x 74 mm large with 1 mm on the edges which is not sensitive. The segmentation is of 768 strips on each side with a pitch of 95 μm. The silicon bulk is n doped, one side is segmented in p strips (P side) and the other in n^+strips (N side), both readout by capacitive coupling. On both sides of the detector, the strips are inclined by ± 17.5 $mrad$ with respect to the short side of the detector, leading to a stereo angle of 35 $mrad$.

2.2 Test beam setup

We performed, in collaboration with LEPSI (Strasbourg) and IReS (Strasbourg), two different tests, one in May 1998 at the SPS with 120 GeV/c pion beam, and one in August 1998 at the PS delivering pions with energies between 1 and 6 GeV. We used 8 single sided silicon strip detectors as reference detectors : 4 in each direction in the plane perpendicular to the beam (figure 2). The reference detectors have a pitch of 50 μm with floating strips. The Coulomb multiple scattering and the resolution of the reference detectors contribute to the resolution measured on

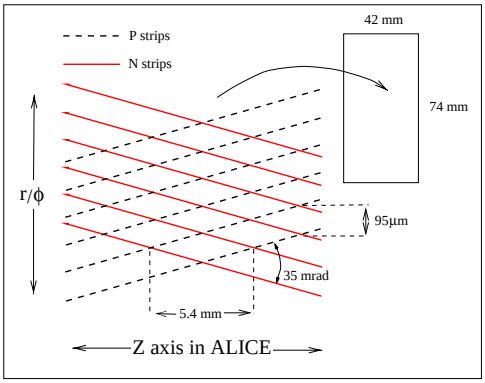

Figure 1: Schematic view of the double-sided microstrip detector

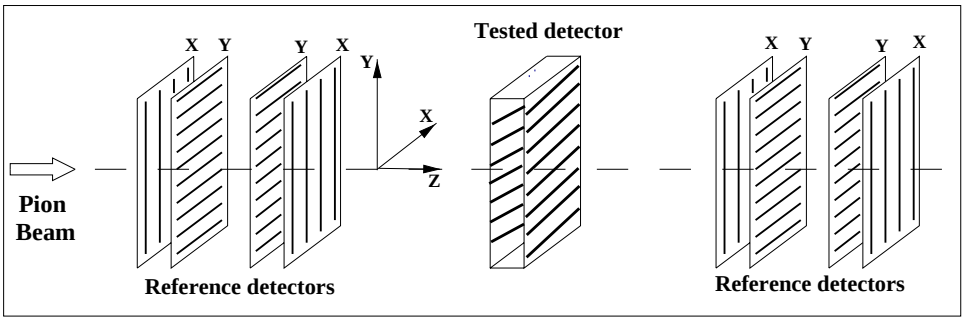

Figure 2: Schematic view of the experimental setup.

the tested detectors. These contributions were of a few microns during the 120 GeV/c pion beam for all detectors. For the 6 GeV/c pion beam, they were also of a few microns only for the detectors equipped with ALICE 128C which were placed in between the reference detectors while the detectors equipped with VA2 where behind the telescope. In the following, all the spatial resolutions given for the detectors equipped with VA2 have been measured using 120 GeV/c beam data and for the detectors equipped with ALICE 128C chips using 6 GeV/c beam data. Thus, the contributions of the multiple scattering and of the intrinsic resolution of the reference detectors are negligible with respect to the resolutions of the tested detectors. The telescope as well as the DAQ are decribed in [5].

3 Test beam results

In this section we present detailed results obtained with test-beam data. We first analyse P and N side separately and then describe the impact point reconstruction when both sides are associated.

3.1 Single-side performances

3.1.1 Signal, noise and signal-to-noise ratios

The off-line reconstruction has already been described in [2]. We extracted the signal-to-noise ratio by fitting the distributions using a Landau distribution convoluted with a Gaussian one as shown in figure 3 for the Canberra detector equipped with VA2 chips. This method gives a reliable value for the peak of the Landau

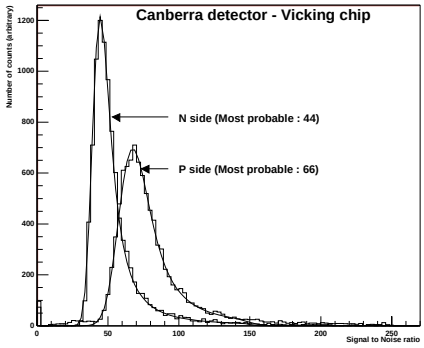

Figure 3: Signal-to-noise distributions of the Canberra detector equipped with VA2 chips during the 120 GeV/c pion beam. The lines correspond to a Landau distribution convoluted with a Gaussian one.

Det. & FEE	Beam GeV/c	S / N P side	S / N N side	Leakage current (μA)
Canb. + ALICE 128	6	42	39	3.1
Canb. + VA2	6	58	39	2.5
Canb. + VA2	120	66	44	2.5
Eur. + ALICE 128	6	59	32	3.6
Eur. + VA2	120	42	26	6

Table 2: Signal-to-noise ratios and leakage currents measured for various detectors and front end electronics. Signal and noise values are given in ADC counts.

distribution, however, we did not study in detail whether the width of the Gaussian is meaningful or not.

The results obtained with the other detectors and FEE are compiled in table 2. The slight differences in signal-to-noise ratios with respect to those reported in [2] for the same detectors, are due to the different methods used to calculate the noise. We used the noise caculated on off-beam channels and assumed that it was the same for in-beam channels, which is true for the detectors equiped with VA2 chips but only approximate for detectors equiped with ALICE 128C chips.

For the 6 GeV/c pion beam, data were collected with both VA2 and ALICE 128C chips connected to a Canberra detector. On the N side, they show the same signal-to-noise ratios while on the P side, the VA2 gives a larger signal-to-noise ratio.

The Eurysis detector with VA2 chips showed a larger leakage current than the detector equipped with ALICE 128C chips which should lead to a larger noise. Thus, the differences in the signal-to-noise ratios of the Eurysis detectors are probably due to the detectors rather than the FEE.

The signal-to-noise performances of the detectors equipped with ALICE 128C chips compare well with those with VA2 chips, which is a good result since the dynamic range of the ALICE 128C chip is twice the one of the VA2.

It should also be noticed that the signal-to-noise ratio is in general 30% lower on the N side than on the P side. This difference is mostly due to a lower signal on the N side than on the P side. This also indicates that for the Canberra detector equipped with ALICE 128C chips, the signal-to-noise ratio on the P side is probably underestimated due to a larger noise than on the other detectors.

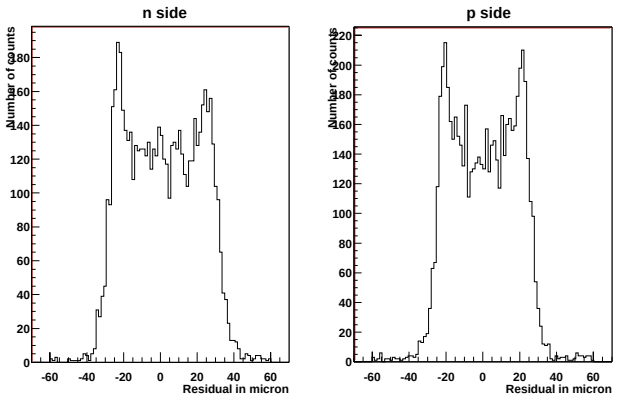

Figure 4: Residuals obtained with the Canberra detector & VA2 Chips. The spatial resolutions are 17.8 μm on the N side and 19.8 μm on the P side.

Detector & FEE	Beam GeV/c	Resolution P side	Resolution N side
Canberra + Alice 128C	6	16.7 μm	21.3 μm
Canberra + VA2	120	17.8 μm	19.8 μm
Eurisys + Alice 128C	6	20.5 μm	22 μm
Eurisys +VA2	120	18.3 μm	21.5 μm

Table 3: Spatial resolutions measured with Canberra/Eurysis detector and ALICE 128C/VA2 front end electronics.

3.1.2 Efficiency

The efficiency of each side is defined as the fraction of events for which we find a cluster in the tested detector which can be associated to the track. It is larger than 98% for all detectors and the few percent missing are due to dead strips.

3.1.3 Resolution at normal incidence

In this section, we study the resolution in the direction perpendicular to the strips on each side, at normal incidence. We first reconstruct the track using the reference detectors and then extrapolate it to the tested detectors in order to localize the impact point. Figure 4 shows the distributions of the distance between the impact point on the tested detector and the positions of the clusters, i.e. the residuals.

Since the shapes of the residual distributions are non-Gaussian, the spatial resolutions are calculated using the RMS with a cut of the maximum residual at 60 μm in order to avoid a large contribution to the RMS of the rare residual values which are wrong.

The spatial resolutions obtained for the various detectors and FEE are quoted in table 3. They are 2 or 3 μm worse on the N side than on the P side which is not fully explained by the differences in the signal-to-noise ratios reported in section 3.1.1. For instance, the signal-to-noise ratio on the N side of the Eurysis detector with VA2 chips was only 26 (table 2) but the spatial resolution is quite comparable to the N side of the other detectors (around 21 μm). Indeed, the signal-to-noise ratios are high enough so that the spatial resolutions are only slightly dependent on them. The detailed phenomena which contribute to the resolution are studied in section 4.

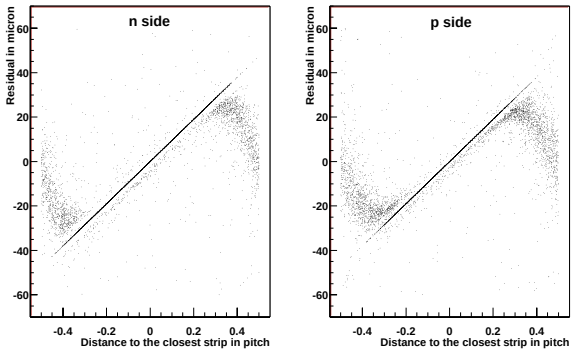

Figure 5: Residual as a function of the distance between the impact point and the closest strip.

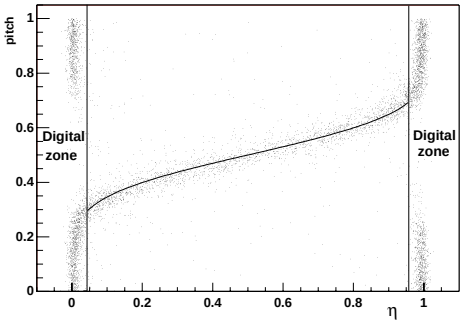

Figure 6: Distance between the hit position and the closest strip on its left–hand side as a function of η.

Figure 5 shows the residual as a function of the distance between the impact point and the closest strip. The clusters made of one strip are visible in the straight line at the center of the figure. Indeed, for clusters with only one strip, the residual is equal to the distance between the impact point and the closest strip.

When the impact point gets further from the central strip (i.e. $|x| > 0.3$ where x is the distance to the closest strip in pitch unit) the clusters start to be made of two strips. In this case, the centroid of the cluster gets closer to the true impact point and the residual goes down to zero when the track crosses the detector at the middle of the inter-strip ($|x| > 0.5$). The two peaks in figure 4 arise from the fact that around x=$\pm$0.3, the residual is almost constant around 20 μm. Since the charge starts to be shared between two strips for a distance of 30 μm from the closest strips, the resolution is much better than the digital one (27 μm) even when using a simple center of gravity algorithm.

3.1.4 Optimisation of the cluster position reconstruction using the η algorithm

The charge sharing between two strips is a non-linear function of the distance between the impact point and the strips. This is measured by $\eta = \frac{S_R}{S_R+S_L}$where S_R (resp. S_L) is the signal on the right-hand side strip (resp. left-hand side strip). In order to estimate the best resolution achievable, we did not apply any cut on

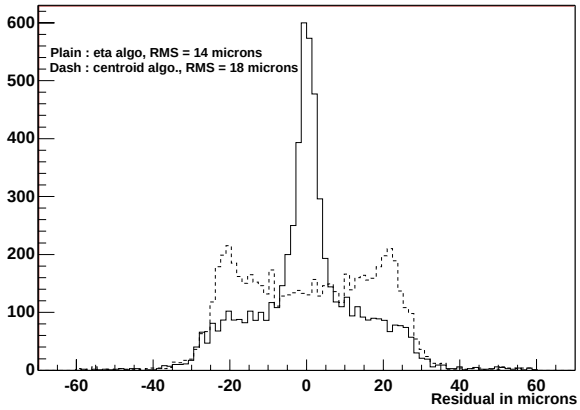

Figure 7: Comparison of the two position reconstruction algorithms : centroid (dashed) and η (plain).

the neighbouring strips, so that all clusters contain two strips at normal incidence. When the whole the signal is collected on one strip, η may be either equal to 0 or 1 depending if the strip which collected the whole signal is the right or the left strip of the cluster. Figure 6 shows the distance x (in pitch unit) between the impact point and the closest strip at the left-hand side as a function of η. For $\eta < 0.04$ and $\eta > 0.96$ (digital zone) the cluster position is equal to the position of the strip which collected almost the whole signal. The width of the digital zone depends on the cut applied on the signal-to-noise ratio of the neighbouring strips. In the non-digital zone, η can be used to reconstruct precisely the position of the cluster instead of using the cluster centroid. Figure 7 shows the residual obtained with the η algorithm and the resolution of 14 μm has to be compared to 17.8 μm obtained with the same data using the centroid algorithm. However, the η distribution should vary with the incident angle, which means that this algorithm could not be used in a first pass. Also, since the detector occupancy should be limited, the neighbouring strips cannot have an arbitrarily low signal, which enlarges the width of the digital zone and hence limits the power of the η algorithm.

3.1.5 Resolution as a function of the incident angle

To study the spatial resolution at non-normal incident angles, we rotated the tested detectors around the X axis (see figure 2). Figure 8 shows the resolution as a funtion of the incident angle using the centroid algorithm. The resolution is the best around 20^o since at this angle the charge is almost always shared between at least two strips making the centroid algorithm efficient. At larger angles, the signal collected on one strip is more sensitive to ionization fluctuations and the centroid algorithm is then less efficient. At smaller angles, the fraction of single strip clusters gets larger which lowers the spatial resolution.

With the simplest algorithm, we finally get a good position resolution at all angles, without assuming that we know the incidence angles.

3.1.6 Two-track resolution

In the ALICE high multiplicity environment, where up to 30 particles per detector may be expected, a very good granularity is required. In order to estimate the two-track resolution along the direction perpendicular to the strips, we summed up

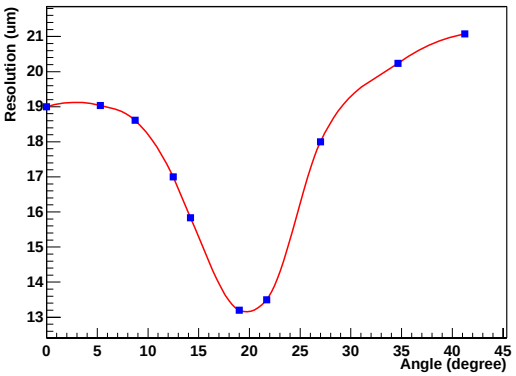

Figure 8: Spatial resolution as a function of the incident angle for the P side of the Canberra detector.

the pulse-height value of two events and then ran the cluster finder algorithm. For each of the two single track event, we know the impact point corresponding to each cluster and thus can calculate the distance between the two impact points.

Figure 9 shows the number of clusters which were actually reconstructed as a function of the distance between the two tracks. The cluster algorithm which was used is adapted from the simplest one in order to look for holes in clusters with more than two strips. Thus, if a strip has a signal lower than 80% of the signal collected by its neighbours, the cluster is split in two.

The two-track resolution obtained with this algorithm (RMS of the distribution for events with one cluster in figure 9) is of the order of 80 μm at normal incidence. This value corresponds to the RMS of a flat distribution between -140 μm and 140 μm which then gives an estimation of the distance required between two tracks to separate them in the direction perpendicular to the strips. However, it should be noticed that the distance between two tracks is not the single parameter to reconstruct two clusters or only one. Indeed, given a distance between two tracks, one or two clusters may be reconstructed depending whether the tracks crossed the detector close to the strips or in the middle-region as schematically shown in figure 10.

We have also checked that at larger incidence angle (30^o), this algorithm does not split a significant fraction of single track clusters since at large incident angle, the clusters may easily have three strips.

This algorithm improves the two-track resolution obtained with the simplest cluster algorithm which just adds to the central strip all the strips having signal-to-noise ratio higher than a given cut. With this new algorithm, we recover 30% of the events for which the simplest algorithm allows to reconstruct only one cluster (with the simplest algorithm, the RMS of the distribution of one cluster events is higher than 100 μm which means that the two clusters have to be separated by one strip).

In this study, we assumed that there is no difference between a real two-track event and two one-track events. The noise is then overestimated by a factor $\sqrt{2}$ but the signal-to-noise ratio remains large enough to make this change not relevant. The other hypothesis is that the charge is collected in the same way if there are two clusters close to each other or only one.

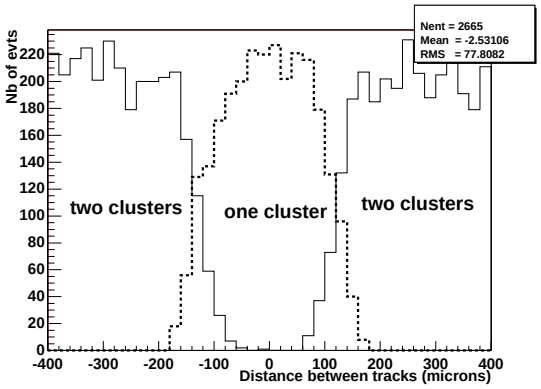

Figure 9: Number of reconstructed clusters as a function of the distance between two tracks.

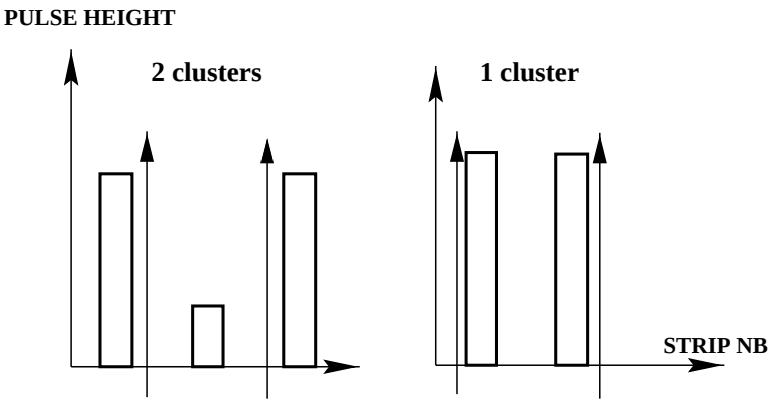

Figure 10: For a given distance between two tracks (arrows) we can reconstruct two clusters (left) or only one (right) depending where they crossed the detector.

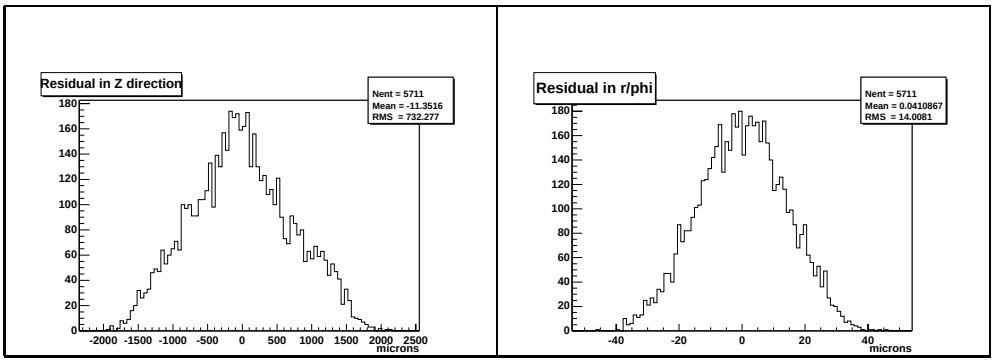

Figure 11: Residual in Z and (r/φ) directions.

3.2 Reconstruction of the impact point using both sides of the detector

In this section, we describe the performances of the detector in terms of spatial and energy deposit resolutions when the clusters reconstructed on P and N sides are associated.

3.2.1 Spatial resolutions

In order to reconstruct the coordinates of the impact point in the local reference frame of the detector (i.e. in the (X,Y) plane in figure 1), one has to associate the clusters reconstructed on each side of the detector. The Z axis of the ALICE experiment corresponds to the X axis in figure 1 and the (r/φ) coordinate (in the transverse plane of the ALICE experiment) correspond to the Y axis of figure 1. Figure 11 shows the residuals for the Z coordinate and for the (r/φ) coordinate. The measured resolutions usign the centroid algorithm (σ_Z =750 μm and $\sigma_{r\varphi}$=14 μm) correspond to the values expected for a stereo angle of 2^o and an intrinsic resolution on each side around 20 μm.

A feature which does not appear on the residual distributions is that, in particular at normal incidence, the impact points measured are located mostly at the crossings between strips of P and N side (when the clusters on each side have one strip) or along the strips (when the clusters are made with one strip on one side and two strips on the other side). This is due to the low fraction of events with a cluster size of 2 strips on both P and N sides. Figure 12 shows the distribution of the impact points reconstructed around the crossing between one P strip and one N strip .

The resolutions along Z and (r/φ) are thus functions of the distance between the impact point and the closest P-N crossing point as shown in figure 13.

3.2.2 Study of the charge correlation between P and N sides.

Double-sided detectors present various advantages compared to back-to-back single-sided detectors : less radiation length, automatic alignment of both sides within 5 μm and correlation between the charge measured on P and N sides. This last feature is useful in the framework of high multiplicity environment. Indeed, the charge correlation helps solving ambiguities inherent to the use of intrinsically single-sided detectors with a stereo angle (i.e. P and N sides).

Figure 14 shows the correlation between the charges measured on P and N sides. The straight line, corresponding to the best matching, is determined minimizing the sum of residuals for all measured points.

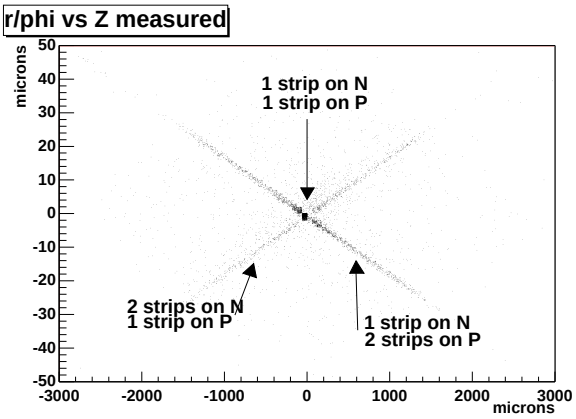

Figure 12: Impact points recconstructed around the crossing point between P and N strips.

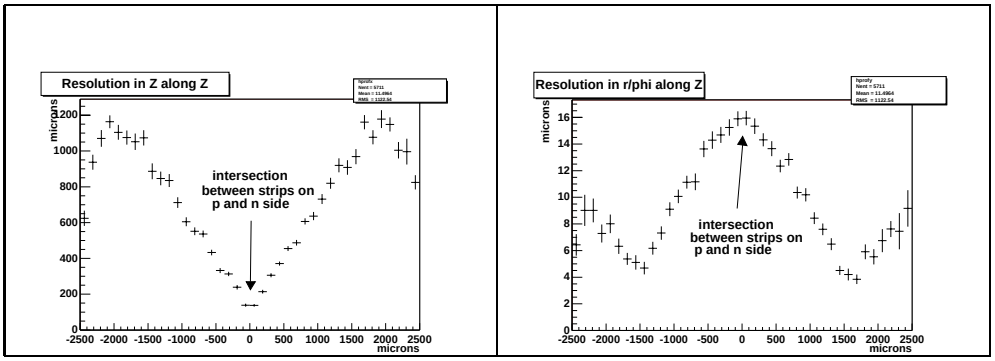

Figure 13: Resolution in Z and (r/φ) as a function Z_{impact} where Z_{impact}=0 corresponds to the crossing between P and N strips.

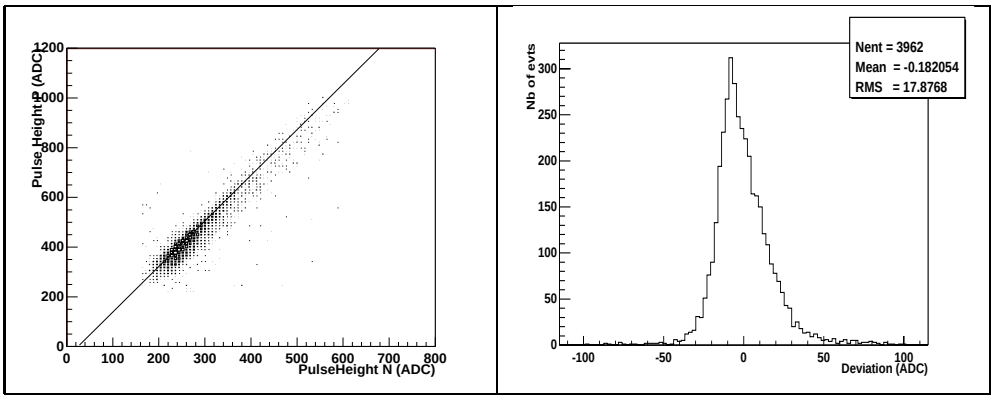

Figure 14: Correlation between the charges measured on P and N sides. The figure on the left side shows the charge measured on the P side as a function of the charge measured on the N side with a straight line corresponding to a fit. The figure on the right shows the distribution of the residuals of this fit.

The fact that the fit does not cross the origin and the non-Gaussian shape of the residual distribution are due to systematic effects in the measurement of the charge deposits :

- when a cluster is reconstructed with most of the signal on a single strip, the fraction of signal on the neighbouring strip is taken into account only if it is larger than a S/N cut so that we systematically underestimate the pulse-height of the cluster (except if the whole signal is really collected on one strip, which happens only in the neighbourhood of the strips).
- when a cluster is reconstructed with two strips, the signal is shared between two strips but the noise of each strip contributes so that the resolution on the charge is not the signal divided by the noise of one strip.
- the signal-to-noise ratio is not the same on P and N sides, so that the two previous effects do not lead to the same results on both sides.

Figure 15 shows the distribution of the residual depending on the number of strips in P/N clusters. We clearly see that the deviation from perfect matching not only depends on the electronic noise but also on the number of strips in the cluster. It is the sum of the four distributions of figure 15 which explains the shape of the distribution in figure 14.

4 Simulation of the silicon strip detector and comparison with data

4.1 Model of the charge sharing process

We have developed a simple model to describe the charge sharing between the strips which shows that only the charge carrier diffusion and the capacitive coupling of the strips after the charge collection are relevant. Indeed, since we use charge amplifiers, the pulse-height of a cluster is not sensitive to current fluctuations arising while the charge carriers drift through the silicon bulk but only to the amount of charge collected by each strip. The charge carriers scatter along their path through the silicon bulk and the diffusion of the holes and electrons can be modelized by a

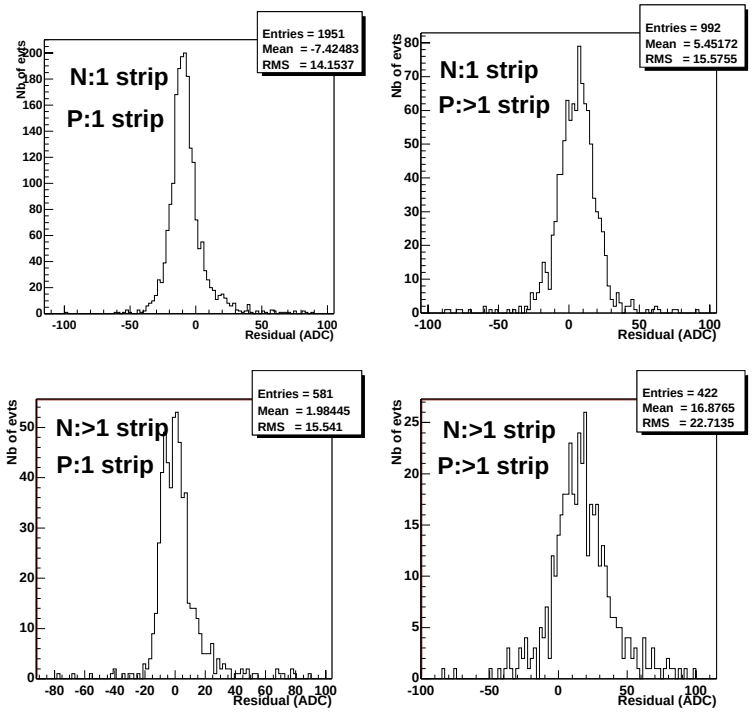

Figure 15: Deviation from the best matching when associating P and N clusters with N^n_{strip}=1 and N^p_{strip}=1 (upper left), N^n_{strip}=1 and N^p_{strip}>1 (upper right), N^n_{strip}>1 and N^n_{strip}=1 (lower left), N^n_{strip}>1 and N^p_{strip}=1 (lower right).

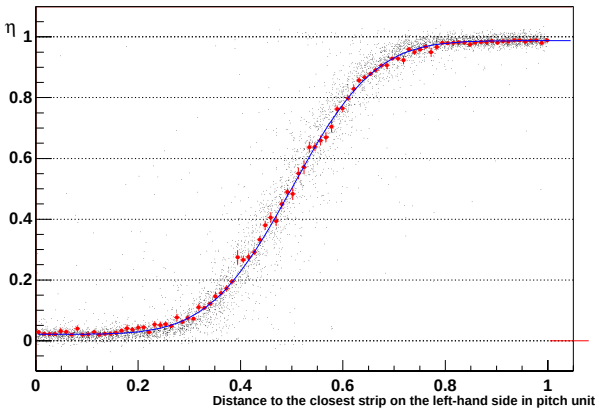

Figure 16: η as a function of the distance between the impact point and the closest strip. Points correspond to data and the line to a fit using the model.

Gaussian distribution with a width $\sigma = \sqrt{\frac{kT}{E}x}$, where k is the Boltzmann constant, T the temperature, E the electric field and x the drift distance. In our model, we considered only the drift distance along the depth of the detector neglecting the longitudinal diffusion. For the maximum drift distance of 300 μm, this σ is of the order of 20 μm and thus, the diffusion plays a role only for tracks crossing the detector around the middle of two strips.

When a strip collects a charge Q_{col}, it induces a signal on its neighbours equal to $Q_{neigh} = \frac{Z_{neigh}}{Z_{col}+Z_{neigh}}.Q_{col}$ where Z_{neigh} (resp. Z_{col}) is the impedance from the collecting point to the ground through the neighbouring (resp. collecting) channel. When only one strip collects the whole charge Q_{tot}, the capacitive coupling $C = \frac{Z_{neigh}}{Z_{neigh}+Z_{col}}$ is equal to $\frac{Q_{neigh}}{Q_{tot}}$.

4.2 Comparison with data

In this model, η can be expressed as a function of the distance to the closest strip. Figure 16 shows the distribution of the measured points and a fit performed with this model which reproduces quite well the data (here $\eta = \frac{S_R}{S_R+S_L}$ where S_R is the signal on the closest strip at the right-hand side of the impact point and S_L the signal on the closest left-hand side strip).

However, some effects do not appear on this figure. In order to go further in the comparison between the model and the data and try to estimate the diffusion and the capacitive coupling, we studied S_{right}/S_{cent} (resp. S_{left}/S_{cent}) which is the ratio of the signal measured on the right-hand side strip (resp. left-hand side strip) to the signal of the central strip (i.e. the closest to the impact point). Figure 17 shows the average values of both ratios as a function of the distance between the impact point and the closest strip for the P side of the Canberra detector equipped with VA2.

Using our model, these two distributions should be fitted by the function :

$$f(x) = C + \frac{Q_{neighbour}}{Q_{closest}} = C + \frac{\int_x^{+\infty} \frac{1}{\sqrt{2\pi}\sigma} e^{\frac{(0.5 \pm u)^2}{2\sigma^2}} du}{\int_{-\infty}^{x} \frac{1}{\sqrt{2\pi}\sigma} e^{\frac{(0.5 \pm u)^2}{2\sigma^2}} du}$$

where C is the coupling constant and σ the diffusion constant averaged over the path of the detector. When the distance between the impact point and the closest strip is lower than 0.2 pitch, the whole charge is collected by one strip. In

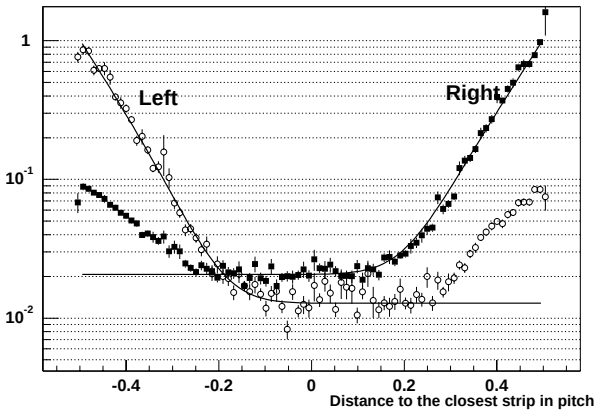

Figure 17: S_{right}/S_{cent} and S_{left}/S_{cent} as a function of the distance to the closest strip.

this case, the left and right strips get signal only by capacitive coupling and we can then extract the parameter C. It appears that the value of C is not the same for the left and right-hand side strips as shown in figure 17. This is probably due to the fact that the analog output is not fully discharged when switching from a channel to the next. To check this, we have used a continuous trigger so that there is always a signal in the analog output. We have then observed an increase of the pedestals which confirms that the tail of the signal of one channel contributes to the signal of the next one. When taking data, the analog output has enough time to be fully discharged between two triggers, so that we do not observe any pedestal increase. The measured value of C is of the order of a few percent, and the observed asymmetry is then not an issue, even if it should be taken into account for position algorithms like head and tail which can be used at larger incident angles.

When the impact point gets closer to the left (resp. right) strip, S_{left}/S_{cent} (resp. S_{right}/S_{cent}) increases. This is well reproduced by the ratio of the two Gaussian integrals which means that it is sufficient to consider the charge carrier diffusion to explain the charge sharing for the particles crossing the detector between two strips. The extracted width of the Gaussian represents the average diffusion over the whole detector depth and could be related to the diffusion coefficient if the electric field in the detector is known precisely.

In figure 17, we also see that S_{left}/S_{cent} (resp. S_{right}/S_{cent}) is not fitted in the region where the particles passed through the detector at a distance larger than 0.2 pitch from the central pitch in the direction of the right (resp. left) strip. This effect shows up only on the P side and has not been explained. It could be due to a second neighbour coupling, but it is rather strong and it can be reproduced only if the second neighbour coupling constant is at the same level than for the first neighbour (i.e. C). Such an effect may be due to the pad connection pattern, which is in staggered rows and then, bondig wires of even and odd strips have the same length and face to each other. However, even if not fully understood, this effect plays a negligible role on the overall performances of the detector.

In section 3.1.4 we have shown how to use the measured distribution of η to optimize the reconstruction of the cluster position, which does not require any model, however the fitting function of figure 16 may also be used to get the same performances.

Table 4 shows the parameters extracted from the fits for the Canberra detector with VA2 chips. The diffusion constant on the N side is lower than on the P side

Detector type	Diffusion constant	Right-hand neighbour coupling	Left-hand neighbour coupling
Canb + VA2, P side	12.3 μm	0.021	0.013
Canb + VA2, N side	9.4 μm	0.026	0.010

Table 4: Parameters of the model extracted from a fit of the data.

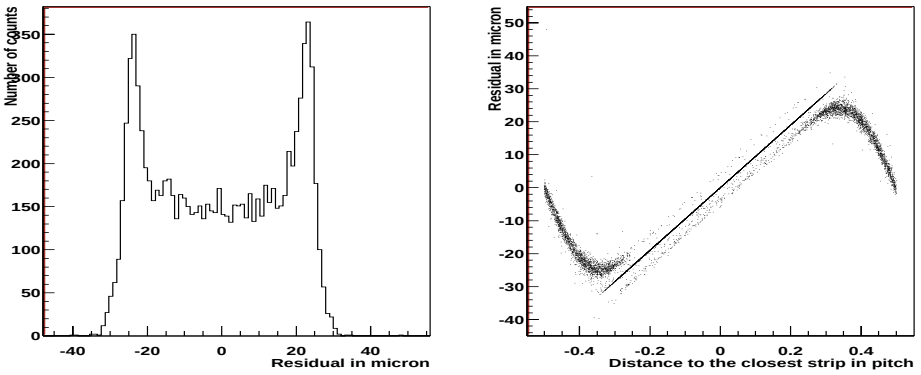

Figure 18: Residual (left) and residual as a function of the distance to the closest strip (right) obtained with a simulation based on the model.

which means that the electrons diffuse less than the holes and hence the charge is less shared between two strips on the N side than on the P side. This explains why the spatial resolution is lower on the N side than on the P side even if the signal-to-noise ratios are equal since a lower diffusion constant means a larger digital zone.

A parameter which could explain different diffusion constants for holes and electrons is the electric field since the mobility cancels out in the diffusion constant expression. The charge carriers created far from the strip where they are collected contribute the most to the diffusion since they drift along the largest distance. Furthermore, close to the N strips for the holes and P strips for the electrons, the charge carriers drift in defocusing field lines which makes the diffusion effect stronger. The diffusion is thus largely due to the charge deposited in these two zones. The electric field is stronger close to the P side than close to the N side due to the P-N junction additional field. Thus, the electrons leave faster the diffusion sensitive zone than holes on the opposite side, making the average diffusion constant measured on the N side lower than on the P side.

4.3 Results of the simulation

Both the charge carrier diffusion and the capacitive coupling have been implemented in a simulation code of the silicon strip detector. Depending on the GEANT routine used for the energy loss, there are some discrepancies with our data which have not yet been studied in detail. However, they affect weakly the spatial resolution. Figure 18 shows the residual distribution and the residual as a function of the distance of the hit to the closest strip obtained with this simulation. For both plots, normal incident 120 GeV/c pions have been generated and the shapes of both distributions agree well with those of figure 5 which shows that the main characteristics of the detector can be efficiently simulated with this simple model.

5 Conclusion

Canberra and Eurysis silicon strip detectors designed for ALICE have been tested using SPS and PS beam data.

The analysis shows good performances of the detectors : spatial resolution is much better than the digital one at any incident angle and efficiencies are higher than 98%.

We have optimized the reconstruction algorithms to get the best spatial resolution that can be achieved with these detectors ($14\mu m$ at normal incidence) and also to minimize the two-track resolution.

The performances of the detectors when associating both sides to reconstruct impact points coordinates have been studied. The spatial resolutions ($\approx 750\mu m$ along Z and $14\mu m$ in the transverse plane at normal incidence) are satisfactory with respect to the requirements of the ALICE experiment. The charge correlation distribution, which is a feature of double-sided detectors, has been studied in details in order to understand systematic effects.

We have developped a simple model to describe the detector behaviour which takes into account the diffusion of the charge carrier and the capacitive coupling between strips. We compared this model to the data and extracted these two parameters which in turn allowed us to perform a realistic and efficient simulation of the detector.

Acknowledgments

We thank our collegues from IReS (Strasbourg) for providing us with the data collected on the detectors equiped with ALICE 128C chips and for the leakage current measurements on these detectors. We would like to thank W. Dulinski for providing us with his test-beam setup. We also thank Dirk Meier (RD42 collboration) for providing us with his off-line analysis code.

References

[1] ALICE Technical Proposal, CERN/LHCC 95-71, LHCC/P3 December 1993

[2] C. Suire et al., ALICE internal note INT-99-22

[3] O. Toker et al., CERN-PPE-93-141

[4] J.R Lutz et al., Proc. of 4^{th} workshop on electronics for LHC experiments, Rome (1998)

[5] C. Colledani et al., NIM A382 (1996) 379